# Self-Interference of Exciton Emission in Organic Single Crystals Visualized by Energy-Momentum Spectroscopy

Christian Schörner,[†,‖] Sajedeh Motamen,[‡] Laurent Simon,[§] Günter Reiter,[‡] and Richard Hildner[*,†]
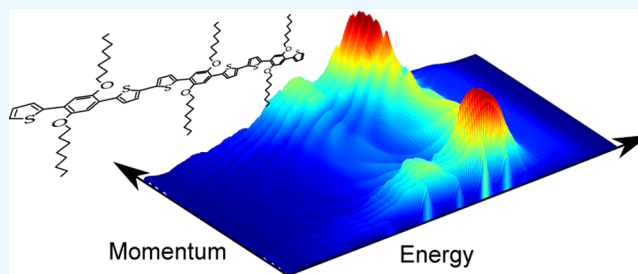
[†]Soft Matter Spectroscopy, University of Bayreuth, Universitätsstr. 30, 95447 Bayreuth, Germany

[‡]Institute of Physics, University of Freiburg, Hermann-Herder-Strasse 3, Freiburg 79104, Germany

[§]Institut de Sciences des Matériaux de Mulhouse IS2M, LRC 7228-CNRS-UHA, 4 rue des frères Lumière, 68093 Mulhouse, France

**S** Supporting Information

**ABSTRACT:** We employ energy-momentum spectroscopy on isolated organic single crystals with micrometer-sized dimensions. The single crystals are grown from a thiophene-based oligomer and are excellent low-loss active waveguides that support multiple guided modes. Excitation of the crystals with a diffraction-limited laser spot results in emission into guided modes as well as into quasi-discrete radiation modes. These radiation modes are mapped in energy-momentum space and give rise to dispersive interference patterns. On the basis of the known geometry of the crystals, especially the height, the characteristics of the interference maxima allow one to determine the energy dependence of two components of the anisotropic complex refractive index. Moreover, the method is suited to identify the orientation of molecules within (and around) a crystalline structure.

## INTRODUCTION

Organic micro- and nanostructures attract great attention in fundamental as well as applied research.[1,2] Many applications have been established, e.g., displays, field effect transistors, waveguides,[3−5] and Mach−Zehnder interferometers.[6] Low-loss waveguiding in cavity-like organic nanostructures has enabled laser operation based on fluorescent[7−10] or on phosphorescent transitions.[11]

Inside such micro- and nanostructures, organic molecules are arranged in a highly ordered fashion and are thus in close proximity to each other. This well-defined, tight packing enables coherent coupling between molecules,[12−14] transport of excitons on ultrafast timescales[15] and over long distances.[16] The spontaneous emission of organic molecules, which are arranged within these structures, and the available optical modes of the structures couple. In the strong coupling regime, the emission becomes reversible and energy is periodically exchanged between light and matter,[17] which strongly depends on material properties. This regime is usually achieved by exploiting microcavities[18] and is currently under investigation exploiting organic dye nanofibers,[19] single-crystal micro-cavities,[20] J-aggregate-doped waveguides,[21] among others. By contrast, in the weak coupling regime, which is relevant in this study, the rate of spontaneous emission is modified by the local density of optical states. Hence, the radiation characteristics of emitters within micro- and nanostructures are a complex function of emission energy and direction.

A very powerful method to directly map the directivity of the emission is back-focal-plane imaging.[5,22−24] The back focal plane of an objective is the Fourier plane of its real space front focal plane, where the sample is located. Thus, it is possible to distinguish the in-plane photon momenta of the emission, i.e., the projections of the momentum on the sample plane, which yields directly information about radiation direction. This technique also allows one to map interference effects of multiple coherently prepared but spatially separated emitters.[25] The back-focal-plane imaging can be expanded to energy-momentum spectroscopy, where not only the radiation direction but also the energy of the emission is recorded.[26−29] Thus, two-dimensional intensity maps with an energy and an in-plane momentum axis result. In addition, this technique can be combined with wide-angle[30] and time-resolved detection schemes.[31]

A full description of light propagation in organic structures, especially in waveguides, requires a continuum of radiation modes and a discrete number of guided modes. Radiation modes are not completely confined in the waveguide and typically leak into the adjacent medium with the highest refractive index, e.g., a glass substrate. In contrast, light in a guided mode propagates along the waveguide by sequential total internal reflection at the boundaries, which completely confine the light inside the organic structure. A key parameter to describe optical waveguides is their refractive index, because, together with the geometry of the entire system (waveguide and surrounding media), it defines the available transverse electric and transverse magnetic waveguide modes. However,
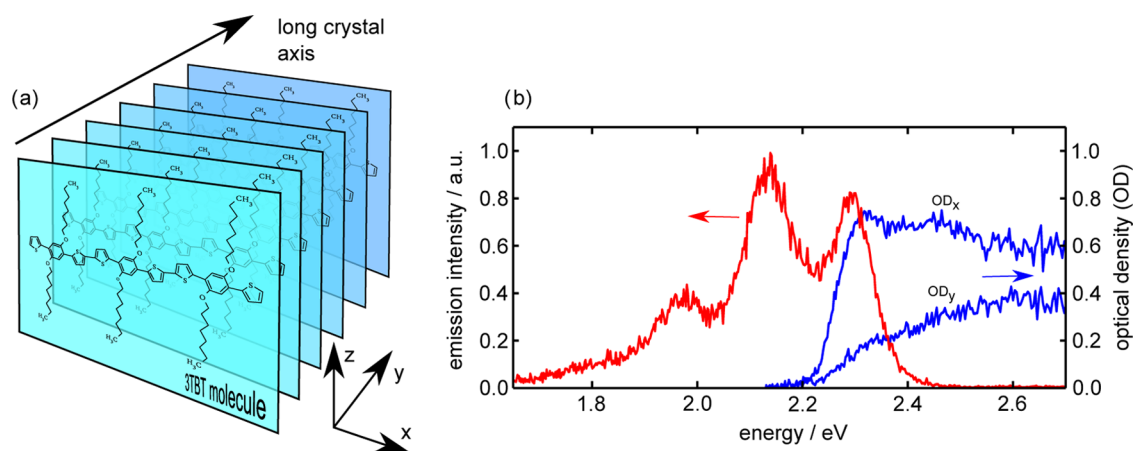
**Figure 1.** (a) Sketch showing the chemical structure of the 3TBT molecules and their arrangement in the single crystals.[5,39] The $x$ direction denotes the orientation of the molecules' backbone, whereas the $y$ direction is the long axis of the crystal, along which adjacent molecules are stacked in a $\pi-\pi$ fashion. (b) Emission (red) and absorption (blue) spectra of 3TBT single crystals. To demonstrate the anisotropy in absorption, the spectra were acquired with $x$- and $y$-polarized light ($OD_x$ and $OD_y$).

the determination of refractive index components of such typically micrometer-sized organic structures is challenging, because they are typically highly anisotropic, which is relevant for a detailed understanding of light propagation.[3,32]

To determine the refractive index components of organic waveguides, several approaches exist: First, the components can be guessed,[10] which, however, can be inaccurate. Second, a group refractive index can be determined via Fabry–Pérot resonances present in the outcoupled spectrum of cavity-like nanostructures.[4,6,19] This method only yields an effective group refractive index for the investigated waveguide mode. The refractive index itself cannot be determined, because the propagation angle of the mode remains unknown. Third, the components can be inferred from angular-resolved, polarized transmission and reflection spectra.[33] The drawback of this method is that for isolated micrometer-sized object, these spectra can be distorted by diffraction. Finally, for flat layers, a common method to determine the refractive index is ellipsometry, but spot sizes down to the micrometer scale require sophisticated imaging spectroscopic ellipsometry.[34−36]

Here, we report a method to determine the complex refractive index components of isolated, well-defined micrometer-sized organic single crystals by fitting energy-momentum spectra with an ensemble of radiating electric dipoles in a multilayer geometry. Our approach is based on self-interference of the emission of crystals that support multiple propagating modes. In the far field, self-interference results in a complex intensity pattern in energy-momentum space, which features a dispersive shape of the interference maxima and can be related to the number of propagating (substrate) modes.

## RESULTS AND DISCUSSION

**Crystal Structure and Optical Properties of 3TBT Single Crystals.** The organic single crystals studied here are based on so-called 3TBT molecules (Figure 1a). Each molecule consists of a sequence of three TBT monomers,[37] with each monomer having a central dialkoxybenzene unit (denoted by B) with two octyl groups attached orthogonally to the backbone of the molecule. The dialkoxybenzene unit is sandwiched by two thiophene rings (denoted by T). The growth of 3TBT single crystals is driven by $\pi-\pi$ interactions between the conjugated backbones of the 3TBT molecules.

Hence, the crystals possess an elongated geometry with one dominant long axis ($y$ direction, Figure 1a), and the 3TBT backbone ($x$ direction) is oriented perpendicularly to this long axis. Figure 1b shows the optical properties of the 3TBT crystals. The absorption is highly anisotropic and is stronger for a polarization parallel to the orientation of the 3TBT backbone as compared to a polarization parallel to the long axis of the crystal. This anisotropy arises from the orientation of the transition dipole moment along the backbone of 3TBT. We note that the absorption and emission does not result from transition dipole moments of 3TBT itself. The close proximity of adjacent, $\pi$-stacked 3TBT molecules gives rise to strong electronic interactions between molecules and thus to the formation of delocalized exciton states. Each exciton state still possesses a transition dipole moment pointing along the $x$ direction, because it is constructed from a weighted vector sum of $x$-oriented 3TBT transition dipole moments.[38]

The emission spectrum of the crystal features a distorted vibronic progression compared to the spectrum of molecularly dissolved 3TBT in solution (cf. Figure 2 in our recent study[39]), which is characteristic for molecules that are arranged in a $\pi-\pi$ (or H-type) fashion.[40,41] The mean energy difference between the vibronic peaks is about 0.17 eV and indicates coupling to carbon-bond stretch modes. The emission strongly overlaps with the absorption around 2.3 eV, which gives rise to substantial reabsorption of the light emitted from within the crystal. To suppress the influence of reabsorption on the emission spectrum as much as possible, we collected only emission with minimal propagation distance within the crystal by momentum filtering (see Figure S1, Supporting Information (SI) for details). More details concerning the crystal structure, as well as absorption and emission of 3TBT molecules in solution, thin film, and single crystals can be found in our recent study.[39]

Figure 2a shows an atomic force microscope (AFM) image of a part of the 3TBT single crystal considered in the following. The topography confirms a nearly homogeneous width of about 4.5 $\mu$m and a height of about 3.3 $\mu$m only slightly varying with position along the crystal's long axis. This very smooth geometry has recently enabled active waveguiding of the emission generated inside such crystals with a remarkably low loss during propagation over several tens of micrometers.[5]
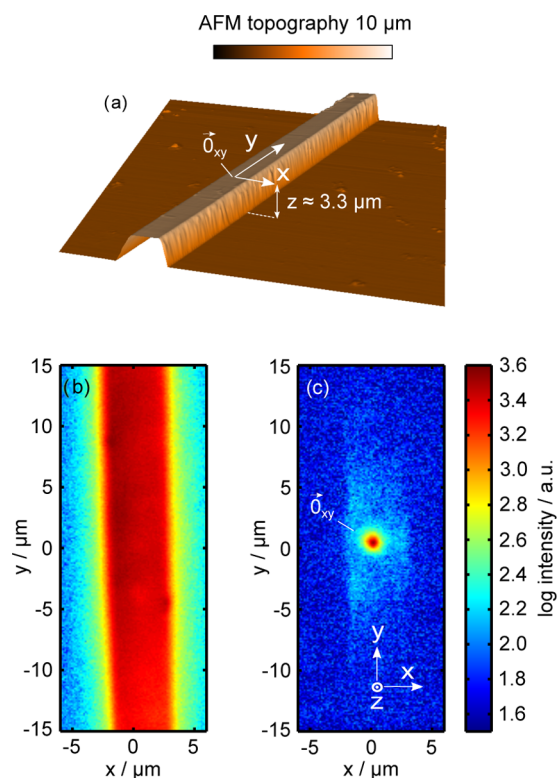
**Figure 2.** (a) Atomic force microscope (AFM) image of a 3TBT single crystal (size $55 \times 55 \ \mu m^2$). (b) Widefield image of the same crystal position as in (a). (c) Emission of the same crystal upon confocal excitation at the position marked with the vector $\vec{0}_{xy}$, see also (a).

Figure 2b displays a widefield image of the same crystal position as shown in the AFM image (after rotation of the crystal to align its long axis ($y$ direction) along the vertical axis of our charge-coupled-device cameras (CCDs)). The crystal shows a bright homogeneous emission on a very low background. Its length along the $y$ direction is several tens of micrometers, whereas the width of the crystal ($x$ direction) is about 4.5 $\mu$m, consistent with the AFM measurement. Figure 2c shows the spatially resolved emission upon confocal excitation of the crystal with a diffraction-limited laser spot at the position marked with the vector $\vec{0}_{xy}$ (see also Figure S2, SI). We observe strong emission at the excitation spot and weaker emission fading away with distance from the excitation spot. We attribute this weak emission to leakage radiation from propagating substrate modes. These emission features can interfere in energy-momentum space as will be demonstrated in the following.

**Fourier Microscopy.** To investigate the directionality of the single-crystal's emission, we exploit back-focal-plane imaging upon local excitation of the crystal at the position marked with $\vec{0}_{xy}$ in Figure 2a,c. In general, the emission in the back-focal-plane image (see Figure S2c, SI) is largely confined within two characteristic circles: an inner circle defined by the total internal reflection condition at the crystal−air interface and an outer circle given by the numerical aperture of our microscope objective, i.e., by the maximum collection angle. Moreover, we observe two emission lobes with in-plane momentum parallel to the $k_y$ direction in Fourier space, which demonstrates directional emission characteristics parallel to the long axis of the crystal ($y$ direction in real space). We attribute

this emission to traveling radiation modes in the crystal leaking into the substrate medium. In addition, there are guided waves totally confined inside the crystal geometry that gives rise to outcoupled emission at the end facets of the crystals, see Figure S1a, SI and ref 5. However, the length of the crystal investigated here does not allow one to detect this signal.

Owing to the pronounced anisotropy of the 3TBT single crystals, with their dominant long ($y$) axis and the orientation of the 3TBT transition dipole moment along the $x$ direction, additional information can be obtained by adding a polarizer in the detection path. In this situation, emission that is polarized perpendicular to the polarizer axis is suppressed. For a polarizer axis oriented in the horizontal ($x$) and vertical ($y$) directions, the back-focal-plane images of the emission are shown in Figure 3a,b, respectively. For horizontal orientation of the polarizer axis, the radiation characteristics show nearly no preferred directions of in-plane momenta (see Figure 3a). There is only one prominent feature in the proximity of $k_x = k_0$ and $k_y \approx 0$ (see black arrow in Figure 3a), i.e., a sideward radiation of the crystal's emission mainly in the positive $k_x$ direction. The asymmetry of this emission can be explained by a slightly shifted excitation position with respect to the center of the crystal, resulting in a symmetry breaking along the $x$ direction. A distinctly different radiation characteristic is collected for a vertical orientation ($y$ direction) of the polarizer axis (Figure 3b). In this case, two distinct radiation lobes can be observed in the positive and negative $k_y$ directions, i.e., along the long axis of the crystal. In particular, there is no emission with $k_y = 0$

The back-focal-plane image acquired with polarizer axis along the vertical ($y$) direction (Figure 3b) appears surprising at the first glance. On the basis of the crystal structure with only $x$-oriented 3TBT molecules (transition dipole moments), we would expect a completely suppressed emission in this situation. In fact, the absence of emission with in-plane momentum parallel to the $k_x$ direction clearly demonstrates that $y$-oriented transition dipole moments are indeed not present in the crystal. Because $x$-polarized emission is suppressed by the polarizer, the emission with in-plane momentum parallel to the $k_y$ direction requires transition dipole moments with a substantial $z$-component. The polarizer modulates the emission intensity of these $z$-oriented transition dipole moments in momentum space with the square of $\cos(\phi - \phi_{pol})$, where $\phi$ is the azimuthal angle in the Fourier plane and $\phi_{pol}$ is the angle of the polarizer axis. Both angles can be measured against an arbitrary reference direction, here the positive $k_x$ axis (cf. Figure 3b). Because of the vertical polarizer axis ($\phi_{pol} = 90°$) and the length of the crystal, $z$-oriented transition dipole moments yield a maximum of the emission in the $k_y$ direction ($\phi = 90°$). The origin of these out-of-plane transition dipole moments can be traced back to the presence of a thin layer of 3TBT nanofibers at the single-crystal surface, which are aligned along the long ($y$) axis of the single crytal.[39] They appear to be randomly twisted around their $y$ axis so that a substantial fraction of emitters with $z$-oriented transition dipole moments is present. Although there could be several layers of nanofibers, the resulting surface roughness is small compared to the wavelength of light,[39] and thus no big deviation from flat single-crystal surfaces considered in our simulations is expected.

The back-focal-plane image with horizontally ($x$-) oriented polarizer axis (Figure 3a) can then be interpreted as emission from a superposition of $x$- and $z$-oriented transition dipole
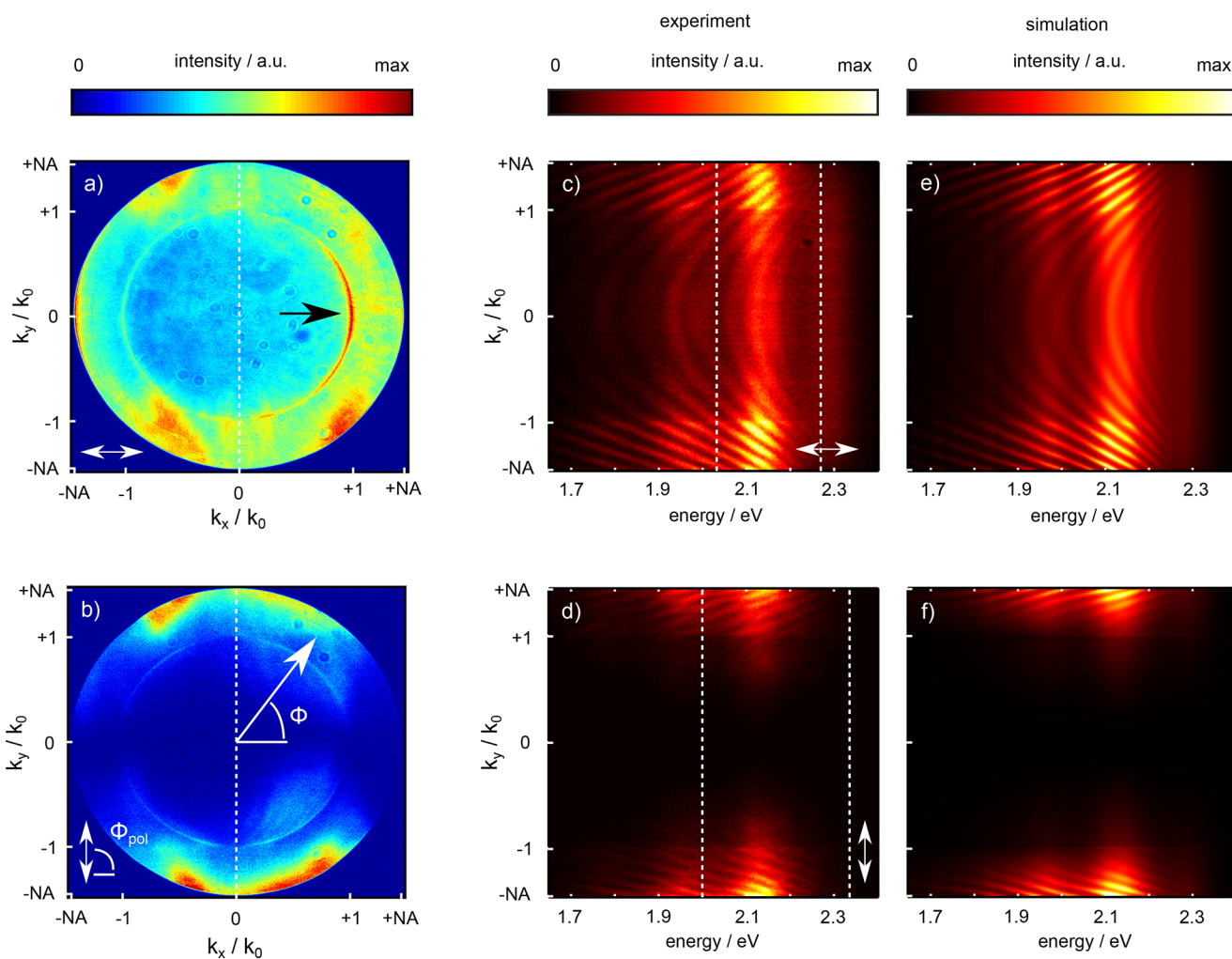
**Figure 3.** (a, b) Back-focal-plane images of the emission upon local excitation of the same single-crystal position as in Figure 2c detected with horizontal ($x$ direction (a)) and vertical ($y$ direction (b)) orientation of the polarizer axis. $\phi$ and $\phi_{pol}$ are the azimuthal angle and the angle of the polarizer axis, respectively, measured against the positive $k_x$ direction. (c, d) Corresponding polarization-resolved energy-momentum spectra with the spectrometer slit along the $y$ direction (cf. white dashed lines in (a) and (b)). The maximum value of the emission in (d) is about a factor of 1.4 higher than that in (c). The dashed lines indicate the energy, along which profiles are shown in Figure 4b,c. (e, f) Simulated energy-momentum spectra.

moments. First, transition dipole moments with orientation in the $x$ direction give rise to emission with in-plane momentum mainly parallel to the $k_y$ direction. Second, according to the above discussion, the modulation of the emission of $z$-oriented transition dipole moments in momentum space results in a maximum emission with in-plane momentum parallel to the $k_x$ direction, if the polarizer axis is along the $x$ direction.

To summarize this section, back-focal-plane images measured with a horizontal polarizer axis ($x$ direction) allow one to detect transition dipole moments oriented along the $x$ and $z$ directions. In contrast, images acquired with a vertical axis ($y$ direction) of the polarizer allow one to detect transition dipole moments exclusively oriented along the $z$ direction, because $y$-oriented transition dipole moments are not present in our 3TBT crystals.

**Energy-Momentum Spectroscopy.** In our recent study we exclusively studied the radiation characteristics of 3TBT crystals.[5] Here we expand our investigation to energy-momentum spectroscopy. Flipping in the Bertrand lens, the back focal plane is imaged onto the plane of the spectrometer entrance slit, which acts as a vertical aperture. Thus, the slit

serves as a vertical intersection through the back focal plane along the $k_y$ direction (dashed lines in Figure 3a,b), and we only collect emission with in-plane momentum $k_x \approx 0$. In combination with a polarizer in front of the spectrometer, we are able to investigate the energy-momentum spectra of $x$-oriented transition dipole moments (polarizer along the $x$ direction) and of $z$-oriented transition dipole moments (polarizer along the $y$ direction), see Figure 3c,d.

For the case of a horizontally oriented ($x$ direction) polarizer axis, several intensity maxima can be clearly observed in the full range from $k_y = -NA \cdot k_0$ to $+NA \cdot k_0$ (Figure 3c). This pattern reflects the emission of the transition dipole moments, placed within the excited crystal volume, into different radiation modes. For $|k_y| > k_0$, we attribute the emission to substrate modes, i.e., radiation modes with losses only into the substrate medium and not into the air above the crystal. These losses are observed in the energy-momentum spectra, and the intensity patterns with distinct maxima and minima reflect the quasi-discrete nature of these modes. The bending of the emission maxima as a function of energy reflects the dispersive behavior of the energy-dependent refractive index (see below).
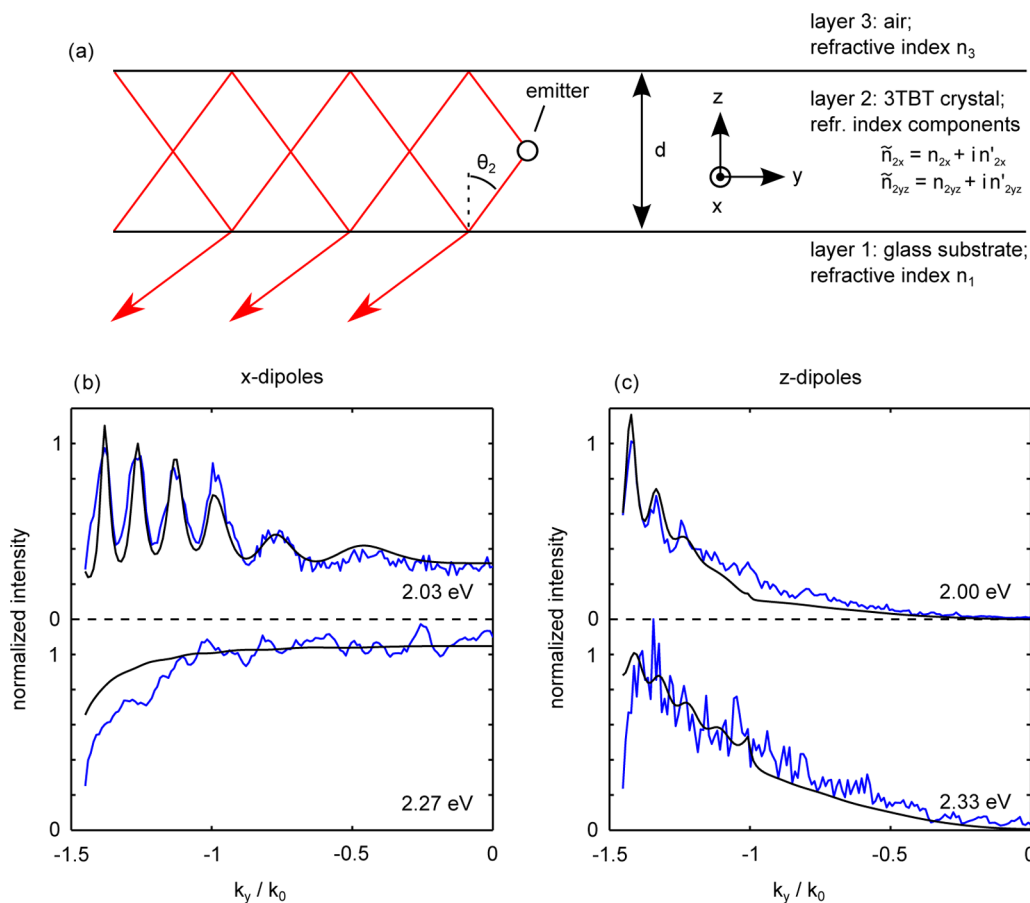
**Figure 4.** (a) Sketch of the sample with its three-layer geometry. Emitters are placed in the 3TBT crystal (layer 2), which is sandwiched between the glass substrate (layer 1) and air (layer 3). For further details, see text. (b) Profiles of the experimental radiation characteristics (blue) extracted at energies of 2.03 eV (top) and 2.27 eV (bottom) from the data in Figure 3c for horizontal orientation of the polarizer axis. The corresponding simulations of $x$-oriented dipole ensembles are shown as black lines. (c) Profiles of the experimental radiation characteristics (blue) extracted at energies of 2.00 eV (top) and 2.33 eV (bottom) from the data in Figure 3d for vertical orientation of the polarizer axis. The corresponding simulations of $z$-oriented dipole ensembles are shown as black lines.

Another way of explaining these patterns is self-interference. The emission sent out from the excitation volume can reach the far field with in-plane momentum $k_\parallel$ through different pathways, see Figure 4a. First, emission can directly leave the crystal medium from the excitation spot and propagate into the substrate. Second, emission can travel to the top 3TBT−air interface, get (partially) reflected, travel back down, and leave the crystal to the substrate. Finally, there are pathways, which include multiple reflections inside the crystal before leaking into the substrate. The emitting transition dipole moment defines the phase of the emission, and thus coherent superposition of all partial waves in the far field (toward the substrate) results in constructive and destructive interference. Hence, the patterns in energy-momentum space map the interference of the emitter's emission with itself. We note that this interference patterns cannot be resolved in the back-focal-plane images (Figure 3a,b) due to the averaging over all energies. Importantly, when the height of the crystal is decreased, we generally observe less fringes (Figure S4, SI), though with similar characteristics. For such thinner crystals, the propagation angle of each mode ($\theta_2$ in Figure 4a) becomes larger, which results in a smaller number of propagating modes available and thus in a smaller number of interference maxima. Thus, the "spacing" between the emission maxima in Fourier space also becomes larger, in agreement with the self-

interference picture. For very thin crystals, we do not observe any fringes (see Figure S1c, SI).

A prominent property of the emission pattern in Figure 3c is that for energies above 2.15 eV, the contrast of the interference pattern decreases rapidly to zero and the distinct fringes disappear. In this energy range, the emission can travel only over very short distances in the crystal due to high reabsorption losses (see Figure 1b and ref 5). Therefore, pathways including multiple reflections are negligible and only the direct path to the substrate remains.

For the case of a vertically oriented ($y$ direction) polarizer axis, we observe a qualitatively similar pattern with several interference maxima in the energy-momentum spectrum (Figure 3d). This pattern is mainly visible in the range of $1 < |k_y|/k_0 < \text{NA}$, consistent with the corresponding back-focal-plane image in Figure 3b. For energies above 2.2 eV, the intensity decreases rapidly to zero, faster than for the case of the horizontal orientation of the polarizer.

**Simulation of Dipoles in the Three-Layer System.** To get insight into the interference patterns, we perform simulations of oriented electric dipoles in a multilayer geometry (layer 1: glass substrate; layer 2: 3TBT crystal; and layer 3: air). A sketch is given in Figure 4a. Importantly, these simulations allow us to determine the anisotropic refractive index components of 3TBT crystals. We use a uniaxial

approximation of the crystal, because we expect a higher polarizability of the electron density along the conjugated backbone of the 3TBT molecules ($x$ direction) compared to the perpendicular ($y$ and $z$) directions. Therefore, the principal axis of the uniaxial medium is taken to be the $x$ axis. The dipole approximation in the simulations is justified by the fact that the emission originates from transition dipole moments of excitonic states that are expected to be delocalized over only a few ($\sim$3) 3TBT molecules in the $y$ ($\pi$-stacking) direction, based on theoretical studies on thiophene-based conjugated polymers.[40] Thus, the spatial extent of the emitting exciton is expected to be very small compared to the wavelength of light. In the simulations, all three media are taken to be infinitely large layers in the $x-y$ plane. The experimental widefield images do not allow one to visualize the entire length of the crystal; hence, it can be considered in good approximation as infinitely long in the $y$ direction. In the energy-momentum spectra, we only collect emission parallel to this $k_y$ direction. Therefore, effects on the energy-momentum spectra due to the finite width of the crystal in the $x$ direction are minimized, and the three-layer approximation allows one to study the main features of the energy-momentum spectra.

The radiation characteristics along the $k_y$ direction into the substrate layer 1, which sensitively depends on the angle $\theta_2$ (Figure 4a), are calculated by reciprocity (see Calculation of Energy-Momentum Spectra, SI) for the considered energy range between 1.65 and 2.4 eV. The substrate layer 1 is modeled with the refractive index of glass ($n_1 = 1.5$) and layer 3 (air above the crystal) with a value of $n_3 = 1.0$. We assume only the real parts of these refractive indices, because these layers are transparent in the relevant energy range. Important parameters for the calculations are the energy-dependent complex refractive index components of the crystal, which are the free parameters for the fitting procedure below. Further crucial parameters are the height of the 3TBT layer 2, which is set to 3.3 $\mu$m according to the atomic force microscope measurement in Figure 2a, and the positions and orientations of the radiating dipole ensembles in layer 2. Given the experimental conditions with focused laser excitation entering the crystal from the substrate medium, for horizontal ($x$ direction) polarizer axis, we use an $x$-oriented dipole ensemble distributed exponentially from bottom to top (3.3 $\mu$m) with an absorption coefficient of 0.3 $\mu$m$^{-1}$ estimated from our earlier study.[39] The pattern obtained with vertical ($y$ direction) polarizer axis originates from $z$-oriented dipole ensembles, which are distributed homogeneously in a 120 nm layer on top of the 3TBT crystal (height 3130−3250 nm, 40 dipoles in total) and a single dipole in 10 nm height at the bottom of the crystal. Note again that $z$-oriented transition dipole moments stem very likely from nanofibers on the surface (top and bottom) of the 3TBT crystals.

A fitting routine is carried out that fits the calculated radiation characteristics of the considered dipole ensemble to the experimental data for each energy using the complex refractive index of the 3TBT single crystal as free parameter (Figure 4b,c). For the $x$-oriented dipole ensemble in the simulation, only the refractive index component along the $x$ direction is relevant and thus allows for an independent fitting of $\tilde{n}_{2x}$ (Figure 4b). Similarly, the $z$-oriented dipole ensemble allows for fitting of $\tilde{n}_{2yz}$ (Figure 4c). In other words, the two independent fitting routines allow one to determine two components of the refractive index of the crystal, namely $\tilde{n}_{2x}$ and an average value $\tilde{n}_{2yz}$ of $\tilde{n}_{2y}$ and $\tilde{n}_{2z}$. The resulting real and

imaginary parts of $\tilde{n}_{2x} = n_{2x} + in'_{2x}$ and $\tilde{n}_{2yz} = n_{2yz} + in'_{2yz}$ are shown in Figure 5a,b, respectively. For energies above 2.3 eV
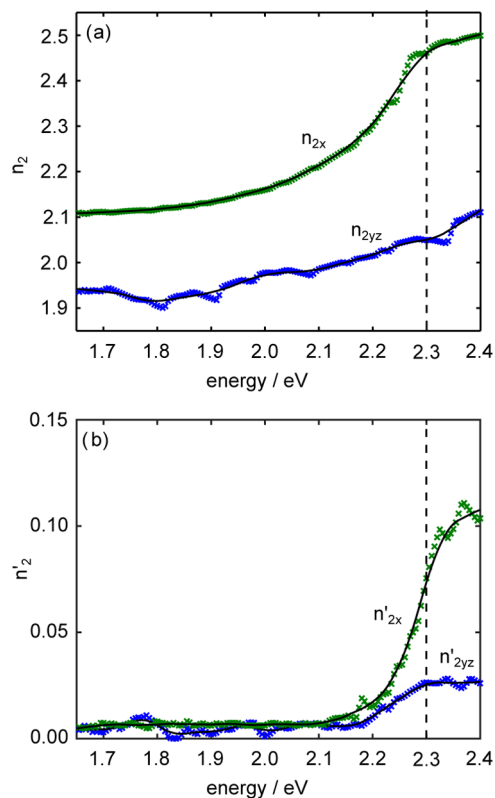


**Figure 5.** Refractive index components obtained from the simulations. (a) Real parts of the crystal's refractive index $n_{2x}$ for the $x$ direction and $n_{2yz}$ for an average in the $yz$ direction. (b) Imaginary parts of the same refractive index components. Black lines represent smoothed values.

(see dashed lines in Figure 5), the fitting becomes inaccurate, because in this range, substrate mode peaks vanish. Their position in $k$-space is the main criterion to fit the real part of the refractive index. Moreover, in this range, the signal decreases drastically, and the fitting becomes inaccurate due to the decreasing signal-to-noise ratio.

The real parts of both refractive index components show a normal dispersion with energy, which is clearly mapped in the interference patterns as a bending of the maxima toward higher $|k_y|$ for increasing energy (cf. Figure 3c,d). Moreover, we find a marked anisotropy due to the high degree of order in the crystal. The fact that $n_{2x}$ is bigger than $n_{2yz}$ is consistent with the structure of 3TBT single crystals, with the backbones of the 3TBT molecules being oriented along the $x$ direction. The real parts of the refractive indices are in the range of about 1.9−2.5, and are in good agreement with the values of thiophene-based systems.[33,42] The imaginary parts are very small for energies below 2.2 eV, where no absorption of the crystal is expected. Possible scattering of the propagating substrate modes, e.g., at interface defects, also leads to an attenuation of the (multiple) reflected lightwaves inside the crystal and thus results in a small imaginary part of the refractive index in the simulation. For energies above 2.2 eV, the imaginary parts strongly increase. The $x$-component is strongest, which is consistent with the anisotropic absorption behavior of the crystal (cf. Figure 1b).

Moreover, the dichroic ratio of $n'_{2x}$ versus $n'_{2yz}$ is consistent with that of the absorption spectra in Figure 1b.

With these refractive index components (smoothed in black), the energy-momentum spectra, especially the dispersive characteristics of the interference maxima, are reproduced very well (cf. Figure 3e,f). The blurring of the pattern in the energy range above 2.2 eV is explained by the increasing imaginary part of the refractive index, resulting in high reabsorption losses of the emission. This prevents multiple reflections of the emission along the crystal, and therefore no substrate/waveguide modes can build up. Note that we weighted the simulated spectra by $\omega^3 |\mu(\omega)|^2$, with the energy-dependent transition dipole moment $\mu(\omega)$ to account for the (distorted) vibronic progression in the experimental data (see Calculation of Energy-Momentum Spectra, SI). Using the refractive index component $\tilde{n}_{2x}$ derived here, we investigated two additional crystals of different sizes. The simulations very nicely reproduce the experimentally obtained energy-momentum patterns only by adjusting the height of the crystal (see Figure S4, SI).

Characteristic profiles of the quasi-discrete substrate modes are shown in Figure 4b,c. In the low-energy range (Figure 4b,c top), several peaks are observed whose full width decreases strongly with increasing $|k_y|$, i.e., radiation angles. In general, the full width at half-maximum (fwhm) of a single propagating substrate mode in $k$-space is related to the propagation length $l_{prop}$ in real space by $l_{prop} = 1/(\text{fwhm} \times k_0)$.[43] In the experiment, we measure fwhm $\approx 0.07$ for the substrate modes with $k_y/k_0 \approx -1.4$ in Figure 4b,c (top). This yields a propagation length of about 1.4 $\mu$m. However, from the emission map in Figure 2c, we calculate a propagation length of about 3.5 $\mu$m in the $y$ direction (see Figure S5f, SI). A detailed analysis reveals that the exact $k_y$-value of the substrate mode depends slightly on the emitter height. Thus, a single emitter defines the minimum width of the substrate mode in $k$-space, whereas an ensemble, which is distributed in height, results in the detection of a broadened width in $k$-space (see Figure S5g–i, SI). By considering the substrate modes of a single emitter, the corresponding propagation lengths are (in average) very close to our experimental observation (see table below Figure S5i, SI). This behavior was verified for two other crystals of different heights (see Figure S5d,e,g,h, SI). In the high-energy range of the energy-momentum spectra, we do not observe any peaks (Figure 4b,c bottom), because the propagation lengths are very short due to reabsorption losses and the signal-to-noise ratio drops down. Finally, we note that the results presented here are reproduced by exclusively assuming propagating substrate modes. Although exciton diffusion over significant distances can occur in organic crystals,[44] we thus conclude that this latter effect is not the predominant mechanism in our system.

## CONCLUSIONS

In conclusion, we have shown that the smooth surfaces of solution-grown single crystals from the organic oligomer 3TBT allow one to observe self-interference of the crystal's emission. We excite the crystal with a diffraction-limited laser spot and bring different pathways of the emitted light wave to interference in energy-momentum space. We note that in our case, we do not have spatially separated coherently radiating emitters, which would also give rise to interference patterns.[45,46] Also, standing wave electric currents radiating from plasmonic nanorods into the far field have been shown to

cause interference patterns.[47] In our case, it is simply 3TBT emitters, confined between interfaces to different optical materials, which give rise to a complex energy-dependent, directional radiation pattern of the crystal. Using a simulation of radiating electrical dipoles in a crystal layer, sandwiched by the substrate and air, we can reproduce the experimentally obtained interference patterns. The fitting allows one to retrieve the anisotropic and complex energy-dependent refractive index components in the crystal (uniaxial approximation), which is a crucial parameter for a detailed modeling of light propagation. Our results are also of high importance for all spectroscopic studies on micro- and nanostructured materials, where real space spectroscopy typically averages over all directions of emission. The emission spectrum of micrometer-sized films and crystals can be distorted in the full energy range due to interferences (see Figure 3c). The strong dependency of the emission spectra on direction is especially important in the high-energy range. The relative strength of the highest energy peak in the emission of $\pi$–$\pi$-stacked organic molecules, such as the 3TBT molecules in a single-crystal arrangement, provides important information about, e.g., the structural order within the structure.[40,41] We found angular-dependent emission spectra even for very thin crystals of about 100 nm in diameter (see Figure S1, SI).

## ■ EXPERIMENTAL SECTION

**Material and Sample Preparation.** 3TBT is 100% regioregular with a molecular weight $M = 1492.32$ g/mol and a contour length of 3.6 nm. As reported recently, micrometer-sized 3TBT single crystals are grown in solution at a relatively high crystallization temperature (60 °C).[5,39] Subsequently, 10 $\mu$L of this solution is spin cast at 1000 rotations/min onto a cleaned glass substrate, so that spatially well-separated single crystals can be optically identified on the substrate. This preparation results in a three-layer geometry of the sample: glass substrate, single crystal, and air.

**Optical Microscopy and Spectroscopy.** The experiments were performed using a home-built optical microscope.[16,48] The excitation source was a pulsed diode laser (LDH-P-C-450B, Picoquant; <60 ps pulse duration) operating at a center wavelength of 450 nm and at 20 MHz repetition rate. The sample is located in the focal plane of an infinity-corrected high numerical aperture (NA) oil-immersion objective (PlanApo, 60×, NA = 1.45, Olympus). This plan-corrected apochromat is ideally suited for Fourier microscopy.[49] The exciting laser light (polarization in the $x$ direction, definition see Figure 2b) can be focused to a diffraction-limited spot with a minimum full width at half-maximum of approximately 350 nm for confocal excitation. By using an additional lens in front of the objective, the sample is illuminated by a beam of about 70 $\mu$m in diameter for widefield imaging. The emission is collected by the same objective and passes a set of dielectric filters (dichroic beam splitter z460RDC, long-pass filter LP467, AHF Analysentechnik) to suppress the laser light. Afterward, the emission is split by a 30/70 beam splitter: 30% of the total intensity is directed to a CCD camera (Orca-ER, Hamamatsu) for imaging and 70% to a spectrometer (SP2150i, Princeton Instruments; 150 grooves/mm, blaze wavelength 500 nm) equipped with a back-illuminated electron-multiplying CCD camera (iXon DV887-BI, Andor Technology).

The back-focal-plane imaging is achieved by flipping in an additional Bertrand lens into the detection path so that the

back focal plane of the objective is imaged onto the CCD camera. For energy-momentum spectroscopy, the back focal plane is imaged onto the spectrometer's entrance slit. The slit acts as an aperture so that only emission with $k_x \approx 0$ (definition see Figure 3a,b) enters the spectrometer. The emission is then dispersed according to its wavelength (energy) and detected by the spectrometer CCD. Note that prior to the measurements, the 3TBT crystals are aligned with their long axis parallel to the entrance slit of the spectrometer by using a pivoted sample mount. A polarizer (Spindler and Hoyer, Polarisationsfilter 80) is placed in the detection path for polarization-dependent measurements.

To measure the absorbance of a 3TBT single crystal, a white light source (Halolux 150, Streppel Glasfaser-Optik) is used to illuminate the sample from top. The transmitted light through the crystal $I_c(E)$ is collected by the microscope objective and detected through the spectrometer as a function of the wavelength (or energy $E$). As a reference, the transmission spectrum $I_{ref}(E)$ is detected at a sample position without crystal. The absorbance is then calculated according to $OD(E) = -\log_{10}(I_c(E)/I_{ref}(E))$.

## ASSOCIATED CONTENT

### ⓢ Supporting Information

The Supporting Information is available free of charge on the ACS Publications website at DOI: 10.1021/acsome-ga.8b00811.

Momentum filtering of the emission spectrum of a 3TBT single crystal (Figure S1); emission maps and back-focal-plane image (Figure S2); calculation of energy-momentum spectra (Figure S3); energy-momentum spectra of different 3TBT crystals (Figure S4); propagation length analysis (Figure S5) (PDF)

## AUTHOR INFORMATION

### Corresponding Author

*E-mail: richard.hildner@uni-bayreuth.de.

### ORCID ⓘ

Laurent Simon: 0000-0002-2627-1525
Richard Hildner: 0000-0002-7282-3730

### Present Address

‖Experimental Physics III, University of Bayreuth, Universitätsstr. 30, 95440 Bayreuth, Germany (C.S.).

### Notes

The authors declare no competing financial interest.

## ACKNOWLEDGMENTS

## REFERENCES

(1) Zhang, C.; Yan, Y.; Zhao, Y. S.; Yao, J. From molecular design and materials construction to organic nanophotonic devices. *Acc. Chem. Res.* **2014**, *47*, 3448−3458.

(2) Zang, L. Interfacial Donor-Acceptor Engineering of Nanofiber Materials To Achieve Photoconductivity and Applications. *Acc. Chem. Res.* **2015**, *48*, 2705−2714.

(3) Balzer, F.; Bordo, V. G.; Simonsen, A. C.; Rubahn, H.-G. Optical waveguiding in individual nanometer-scale organic fibers. *Phys. Rev. B* **2003**, *67*, No. 115408.

(4) Takazawa, K.; Inoue, J.-i.; Mitsuishi, K. Optical Waveguiding along a Sub-100-nm-Width Organic Nanofiber: Significant Effect of Cooling on Waveguiding Properties. *J. Phys. Chem. C* **2016**, *120*, 1186−1192.

(5) Motamen, S.; Schörner, C.; Raithel, D.; Malval, J.-P.; Jarrosson, T.; Serein-Spirau, F.; Simon, L.; Hildner, R.; Reiter, G. Low loss optical waveguiding in large single crystals of a thiophene-based oligomer. *Phys. Chem. Chem. Phys.* **2017**, *19*, 15980−15987.

(6) Takazawa, K.; Inoue, J.-i.; Mitsuishi, K.; Kuroda, T. Ultracompact Asymmetric Mach-Zehnder Interferometers with High Visibility Constructed from Exciton Polariton Waveguides of Organic Dye Nanofibers. *Adv. Funct. Mater.* **2013**, *23*, 839−845.

(7) O'Carroll, D.; Lieberwirth, I.; Redmond, G. Microcavity effects and optically pumped lasing in single conjugated polymer nanowires. *Nat. Nanotechnol.* **2007**, *2*, 180−184.

(8) Zhang, W.; Yao, J.; Zhao, Y. S. Organic Micro/Nanoscale Lasers. *Acc. Chem. Res.* **2016**, *49*, 1691−1700.

(9) Cui, Q. H.; Zhao, Y. S.; Yao, J. Photonic applications of one-dimensional organic single-crystalline nanostructures: Optical waveguides and optically pumped lasers. *J. Mater. Chem.* **2012**, *22*, 4136−4140.

(10) Zhao, Y. S.; Peng, A.; Fu, H.; Ma, Y.; Yao, J. Nanowire Waveguides and Ultraviolet Lasers Based on Small Organic Molecules. *Adv. Mater.* **2008**, *20*, 1661−1665.

(11) Yu, Z.; Wu, Y.; Xiao, L.; Chen, J.; Liao, Q.; Yao, J.; Fu, H. Organic Phosphorescence Nanowire Lasers. *J. Am. Chem. Soc.* **2017**, *139*, 6376−6381.

(12) Zhang, Y.; Luo, Y.; Zhang, Y.; Yu, Y.-J.; Kuang, Y.-M.; Zhang, L.; Meng, Q.-S.; Luo, Y.; Yang, J.-L.; Dong, Z.-C.; Hou, J. G. Visualizing coherent intermolecular dipole-dipole coupling in real space. *Nature* **2016**, *531*, 623−627.

(13) Gierschner, J.; Lüer, L.; Milián-Medina, B.; Dieter, O.; Egelhaaf, H.-J. Highly Emissive H-Aggregates or Aggregation-Induced Emission Quenching? The Photophysics of All-Trans para-Distyrylbenzene. *J. Phys. Chem. Lett.* **2013**, *4*, 2686−2697.

(14) Gierschner, J.; Park, S. Y. Luminescent distyrylbenzenes: tailoring molecular structure and crystalline morphology. *J. Mater. Chem. C* **2013**, *1*, 5818−5832.

(15) Wan, Y.; Guo, Z.; Zhu, T.; Yan, S.; Johnson, J.; Huang, L. Cooperative singlet and triplet exciton transport in tetracene crystals visualized by ultrafast microscopy. *Nat. Chem.* **2015**, *7*, 785−792.

(16) Haedler, A. T.; Kreger, K.; Issac, A.; Wittmann, B.; Milan, K.; Hammer, N.; Köhler, J.; Schmidth, H.-W.; Hildner, R. Long-range energy transport in single supramolecular nanofibres at room temperature. *Nature* **2015**, *523*, 196−200.

(17) Vasa, P.; Wang, W.; Pomraenke, R.; Lammers, M.; Maiuri, M.; Manzoni, C.; Cerullo, G.; Lienau, C. Real-time observation of ultrafast Rabi oscillations between excitons and plasmons in metal nanostructures with J-aggregates. *Nat. Photonics* **2013**, *7*, 128−132.

(18) Tropf, L.; Dietrich, C. P.; Herbst, S.; Kanibolotsky, A. L.; Skabara, P. J.; Würthner, F.; Samuel, I. D. W.; Gather, M. C.; Höfling, S. Influence of optical material properties on strong coupling in organic semiconductor based microcavities. *Appl. Phys. Lett.* **2017**, *110*, No. 153302.

(19) Takazawa, K.; Inoue, J.-i.; Mitsuishi, K.; Takamasu, T. Fraction of a millimeter propagation of exciton polaritons in photoexcited nanofibers of organic dye. *Phys. Rev. Lett.* **2010**, *105*, No. 067401.

(20) Goto, K.; Yamashita, K.; Yanagi, H.; Yamao, T.; Hotta, S. Strong exciton-photon coupling in organic single crystal microcavity

with high molecular orientation. *Appl. Phys. Lett.* **2016**, *109*, No. 061101.

(21) Ellenbogen, T.; Crozier, K. B. Exciton-polariton emission from organic semiconductor optical waveguides. *Phys. Rev. B* **2011**, *84*, No. 161304.

(22) Tripathi, R. P. N.; Dasgupta, A.; Chikkaraddy, R.; Patra, P. P.; Vasista, A. B.; Kumar, G. V. P. Optics of an individual organic molecular mesowire waveguide: directional light emission and anomalous refractive index. *J. Opt.* **2016**, *18*, No. 065002.

(23) Shegai, T.; Miljković, V. D.; Bao, K.; Xu, H.; Nordlander, P.; Johansson, P.; Käll, M. Unidirectional Broadband Light Emission from Supported Plasmonic Nanowires. *Nano Lett.* **2011**, *11*, 706−711.

(24) Gaio, M.; Moffa, M.; Castro-Lopez, M.; Pisignano, D.; Camposeo, A.; Sapienza, R. Modal Coupling of Single Photon Emitters Within Nanofiber Waveguides. *ACS Nano* **2016**, *10*, 6125−6130.

(25) Wolf, D.; Schumacher, T.; Lippitz, M. Shaping the nonlinear near field. *Nat. Commun.* **2016**, *7*, No. 10361.

(26) Taminiau, T. H.; Karaveli, S.; van Hulst, N. F.; Zia, R. Quantifying the magnetic nature of light emission. *Nat. Commun.* **2012**, *3*, No. 979.

(27) Schuller, J. A.; Karaveli, S.; Schiros, T.; He, K.; Yang, S.; Kymissis, I.; Shan, J.; Zia, R. Orientation of luminescent excitons in layered nanomaterials. *Nat. Nanotechnol.* **2013**, *8*, 271−276.

(28) Dodson, C. M.; Kurvits, J. A.; Li, D.; Jiang, M.; Zia, R. Magnetic dipole emission of $Dy^{3+}$: $Y_2O_3$ and $Tm^{3+}$:$Y_2O_3$ at near-infrared wavelengths. *Opt. Mater. Express* **2014**, *4*, 2441.

(29) Li, D.; Jiang, M.; Cueff, S.; Dodson, C. M.; Karaveli, S.; Zia, R. Quantifying and controlling the magnetic dipole contribution to 1.5-$\mu$m light emission in erbium-doped yttrium oxide. *Phys. Rev. B* **2014**, *89*, No. 161409.

(30) Dodson, C. M.; Kurvits, J. A.; Li, D.; Zia, R. Wide-angle energy-momentum spectroscopy. *Opt. Lett.* **2014**, *39*, 3927−3930.

(31) Karaveli, S.; Wang, S.; Xiao, G.; Zia, R. Time-resolved energy-momentum spectroscopy of electric and magnetic dipole transitions in $Cr^{3+}$:MgO. *ACS Nano* **2013**, *7*, 7165−7172.

(32) Takeda, H.; Sakoda, K. Exciton-polariton mediated light propagation in anisotropic waveguides. *Phys. Rev. B* **2012**, *86*, No. 205319.

(33) Egelhaaf, H.-J.; Gierschner, J.; Haiber, J.; Oelkrug, D. Optical constants of highly oriented oligothiophene films and nanoparticles. *Opt. Mater.* **1999**, *12*, 395−401.

(34) Beaglehole, D. Performance of a microscopic imaging ellipsometer. *Rev. Sci. Instrum.* **1988**, *59*, 2557−2559.

(35) Jung, I.; Vaupel, M.; Pelton, M.; Piner, R.; Dikin, D. A.; Stankovich, S.; An, J.; Ruoff, R. S. Characterization of Thermally Reduced Graphene Oxide by Imaging Ellipsometry. *J. Phys. Chem. C* **2008**, *112*, 8499−8506.

(36) Funke, S.; Miller, B.; Parzinger, E.; Thiesen, P.; Holleitner, A. W.; Wurstbauer, U. Imaging spectroscopic ellipsometry of $MoS_2$. *J. Phys. Condens. Matter* **2016**, *28*, No. 385301.

(37) Silva, R. A.; Serein-Spirau, F.; Bouachrine, M.; Lère-Porte, J.-P.; Moreau, J. J. E. Synthesis and characterization of thienylene-phenylene copolymers with oligo(ethylene oxide) side chains. *J. Mater. Chem.* **2004**, *14*, 3043−3050.

(38) Kasha, M.; Rawls, H. R.; El-Bayoumi, M. A. The exciton model in molecular spectroscopy. *Pure Appl. Chem.* **1965**, *11*, 371−392.

(39) Motamen, S.; Raithel, D.; Hildner, R.; Rahimi, K.; Jarrosson, T.; Serein-Spirau, F.; Simon, L.; Reiter, G. Revealing Order and Disorder in Films and Single Crystals of a Thiophene-Based Oligomer by Optical Spectroscopy. *ACS Photonics* **2016**, *3*, 2315−2323.

(40) Spano, F. C.; Clark, J.; Silva, C.; Friend, R. H. Determining exciton coherence from the photoluminescence spectral line shape in poly(3-hexylthiophene) thin films. *J. Chem. Phys.* **2009**, *130*, No. 074904.

(41) Spano, F. C. The spectral signatures of Frenkel polarons in H- and J-aggregates. *Acc. Chem. Res.* **2010**, *43*, 429−439.

(42) Brown, P. J.; Thomas, D. S.; Köhler, A.; Wilson, J. S.; Kim, J.-S.; Ramsdale, C. M.; Sirringhaus, H.; Friend, R. H. Effect of interchain interactions on the absorption and emission of poly(3-hexylthiophene). *Phys. Rev. B* **2003**, *67*, No. 064203.

(43) des Francs, G. C.; Grandidier, J.; Massenot, S.; Bouhelier, A.; Weeber, J.-C.; Dereux, A. Integrated plasmonic waveguides: A mode solver based on density of states formulation. *Phys. Rev. B* **2009**, *80*, No. 115419.

(44) Grover, M.; Silbey, R. Exciton Migration in Molecular Crystals. *J. Chem. Phys.* **1971**, *54*, 4843−4851.

(45) Guebrou, S. A.; Symonds, C.; Homeyer, E.; Plenet, J. C.; Gartstein, Y. N.; Agranovich, V. M.; Bellessa, J. Coherent emission from a disordered organic semiconductor induced by strong coupling with surface plasmons. *Phys. Rev. Lett.* **2012**, *108*, No. 066401.

(46) Dubin, F.; Melet, R.; Barisien, T.; Grousson, R.; Legrand, L.; Schott, M.; Voliotis, V. Macroscopic coherence of a single exciton state in an organic quantum wire. *Nat. Phys.* **2006**, *2*, 32−35.

(47) Hartmann, N.; Piatkowski, D.; Ciesielski, R.; Mackowski, S.; Hartschuh, A. Radiation channels close to a plasmonic nanowire visualized by back focal plane imaging. *ACS Nano* **2013**, *7*, 10257−10262.

(48) Issac, A.; Hildner, R.; Ernst, D.; Hippius, C.; Würthner, F.; Köhler, J. Single molecule studies of calix[4]arene-linked perylene bisimide dimers: relationship between blinking, lifetime and/or spectral fluctuations. *Phys. Chem. Chem. Phys.* **2012**, *14*, 10789−10798.

(49) Kurvits, J. A.; Jiang, M.; Zia, R. Comparative analysis of imaging configurations and objectives for Fourier microscopy. *J. Opt. Soc. Am. A* **2015**, *32*, 2082−2092.